Optimization of the strength of SOFC anode supports

H.L. Frandsen [a,*], T. Ramos [a], A. Faes [b], M. Pihlatie [c], K. Brodersen [a]

[a] *Fuel Cells and Solid State Chemistry Division, Risø National Laboratory for Sustainable Energy, Technical University of Denmark, DK-4000 Roskilde, Denmark*
[b] *Design & Materials Unit, University of Applied Sciences Western Switzerland, CH-1950 Sion, Switzerland*
[c] *VTT - Technical Research Centre of Finland, FI-02044 VTT, Finland*

Abstract

During operation solid oxide fuel cells are stressed by temperature gradients and various internal and external mechanical loads, which must be withstood. This work deals with the optimization of the strength of as-sintered anode supported half-cells by imposing changes to production parameters, such as powder milling and sintering temperature. The strength was measured with the ball-on-ring method, and analyzed with a large displacement finite element model. Weibull statistics were used to describe the distribution of strengths. The influence on the Weibull strength of the many different processing parameters was found to be quantifiable in terms of cell porosity to a large extent. The results were validated with an independent set of measurements of strength and stiffness by uniaxial tension and the impulse excitation technique, respectively. For application of the finding in relation to the SOFC technology a mathematical frame to determine the optimal porosity of a SOFC system is presented.
© 2011 Elsevier Ltd. All rights reserved.

Keywords: Strength; Fuel cells; Sintering; Porosity; Optimization

1. Introduction

One of the main challenges with solid oxide fuel cell (SOFC) technology is to ensure durable and stable operation for higher economical feasibility. Hence, in the development of the technology, a great deal of attention is directed towards cell degradation, integrity of the sealings, and other processes that can affect system efficiency.[1,2] Failure of a cell in a stack will decrease the stack efficiency, as well as shorten the lifetime of the stack considerably. Thus, development should focus not only on electrochemical but also on mechanical performance of SOFCs.

Half-cells consisting of a tape-cast anode support, sprayed YSZ electrolyte, and sprayed Ni/YSZ cermet are already produced on a pre-pilot plant scale at the Fuel Cell and Solid State Chemistry Division, Risø DTU. Lately, in view of the expected advantages, an effort has been made to develop and optimize the manufacturing of fully tape cast half-cells. This offers, at first glance, the possibility of reducing the number of manufacturing steps, as it allows one-step sintering. Also, a reduction of overall production waste makes lower production costs feasible. During

this development, the strength of the cells has been measured as a function of different production parameters. Variations of one or several of these parameters may introduce different flaw distributions, resulting in varying mechanical strength. The strength and indirectly the flaw distribution are typically represented by a Weibull distribution,[3–5] which is also the case for this work.

The present work shows how modification of various production parameters, shaping, sintering temperature, milling period, and material composition influences the strength. The interesting finding is that independent Weibull strength correlates very well to the as-sintered porosity independent of which processing parameter is varied. Thus the porosity can be considered as a convoluting parameter, which accounts for all the processing parameter variations. This is an important observation in relation to production optimization, as this to a great extent can be done in terms of porosity and consequently opens for non-destructive quality testing as the impulse excitation technique.

Another important finding in this work is the high decrease of Weibull strength with porosity, which is only observed in few other ceramics. Thus an independent set of experiments are conducted to confirm the finding, and to test the validity of the non-destructive testing in the production aspect. This is done by measuring the strength with uniaxial tension and the stiffness by the impulse excitation technique.

* Corresponding author. Tel.: +45 4677 5668; fax: +45 4677 5858.
  E-mail address: hlfr@risoe.dtu.dk (H.L. Frandsen).

Table 1
Relevant production parameters for the different tested half-cells series (T1 and T2: type 1 and type 2 additions, CF: 20% ceramic filler; LM, MM and TM: light, medium and thorough milling; LT and HT: low and high temperature; TZ3Y: yttrium partially stabilized tetragonal zirconia, TZ8Y: yttrium fully stabilized cubic zirconia, and ScYSZ: scandium, yttrium fully stabilized cubic zirconia).

Test code	Production method	Materials			Milling: time, powder weight/mill volume	Sintering temperature [°C]	Porosity [%]
		Anode support	Anode	Electrolyte			
SPR T1 HT TM	Spraying				>25 h, <1 kg/L		6.8
SPR T1 HT LM					<25 h, 1 kg/L	>1300	13.7
FTC T1 HT MM		NiO–TZ3Y + T1	NiO–TZ8Y	TZ8Y	>25 h,		11.9
FTC T1 LT MM					1 kg/L		17.4
FTC T2 LT TM 1	Fully tape cast					<1300 °C	9.0
FTC T2 LT TM 2		NiO–TZ3Y + T2	NiO–ScYSZ	ScYSZ	>25 h,		7.0
FTC T2 HT TM					<1 kg/L		4.2
SPR CF HT TM	Spraying	NiO–TZ3 + CF	NiO–TZ8Y	TZ8Y		>1300 °C	12.6

Finally these findings are related to the SOFC technology, where the porosity cannot be decreased unconditionally as the open porosities are allowing for the transport of reacting gasses. The optimum porosity should thus be found by balancing the strength and internal diffusion resistance. A method to weigh the different influencing parameters is discussed in the final section.

2. Experimental

Two sets of experiments have been carried out in this work. The first set of experiments is aimed at quantifying the strength variation with various production parameters, and the second is a combined verification of the first and an investigation of the application of non-destructive methods as described above.

For the first set of experiments the ball-on-ring method was chosen as it provides fast specimen preparation and requires small specimen sizes, so a large number of specimens for the statistical treatment can easily be produced. It is the omission of the polishing process allows for fast specimen preparation. This omission is possible as the failure will not occur at the cut edge, as the stresses here are negligible. This is not the case for many classical test methods (bending methods and uniaxial tension), where careful edge polishing after cutting is required, in order to ensure that the bulk strength is measured.

Due to the dimensions of the testing setup, only a very small volume is exposed to high stresses. This results in a much higher strength for the tested specimens, when compared to full sized cells for stack application, since the probability of significant flaws in the small volume is smaller. A scaling of Weibull strength between so-called efficient volumes is possible according to the Weibull theory. Due to the amount of scaling from the small efficient volumes of the ball-on-ring method to cells in a stack, the results are unsuitable for stack design purposes. However, for comparison of the strength of similar sized specimens, as in the present work, the method is adequate.

For the second set of experiments uniaxial tension was chosen as this also allowed for simple measuring of stiffness by the impulse excitation technique. The impulse excitation technique was chosen over application of strain gauges, as these

can influence both the strength and stiffness measurement of the relatively thin specimens used in this study. The stiffness and strength measurement can be influenced by the stiffness and strength of the gauge itself and by strain gauge glue penetrating the porous specimens.

2.1. Materials and production parameters

For the ball-on-ring experiments, the specimens consisted of as-sintered anode supported planar half-cells. As-sintered anode supports were used for the uniaxial tension experiments.

The half-cells consist of anode support, anode and electrolyte with thicknesses of 300 μm, 20 μm and 10 μm, respectively. The cells were produced either by tape casting/spraying, or solely by tape casting. Powders with different starting characteristics, various milling times/conditions, and different sintering temperatures were used for the different series. Table 1 summarizes all relevant production parameters, including the resulting porosity, for the different test series.

The anode support specimens for the uniaxial tension experiment were produced with the same parameters as the anode support of "SPR T1 HT TM" half cell in Table 1.

The porosities were measured once for each batch with mercury porosimetry (AutoPore IV, Micromeritics, USA).

2.2. Ball-on-ring experiments

In the ball-on-ring experiment the specimens were placed with the electrolyte side up. Hence, the highest tensile stresses (causing the failure) are located at the bottom of the anode support below the ball, where the failure origin consequently occurs. With the opposite orientation the anode support is still the failing component due to the thermal stresses.[6]

The specimens were disc shaped with a diameter of 20 mm and approximately 330 μm thick. The discs were supported by a ring of balls, and loaded by a piston through a ground ball (see Figs. 1 and 2). The diameter of the supporting ring was 16 mm, and the diameter of the flat contact face of the top ground ball (see Fig. 2) had a 2.78 mm diameter.

Fig. 1. Ring of supporting balls and piston for compression (no specimen).
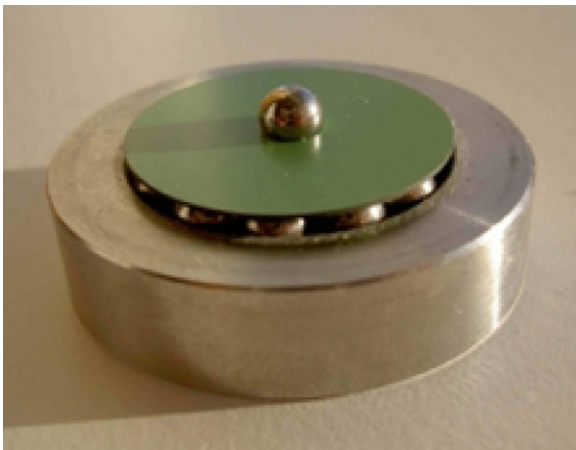

Fig. 2. Specimen on support with the ball centered on top.

The load applying piston was driven by an Instron machine (Model 1362) with a constant displacement rate of 0.2 mm/min. The load was measured with a 250 N or 500 N load cell.

2.3. Uniaxial tension experiments

The specimens for tensile test were anode supports only. Their size was 70 mm × 20 mm, and the thickness was measured for each sample to be between 319 μm and 331 μm. All the
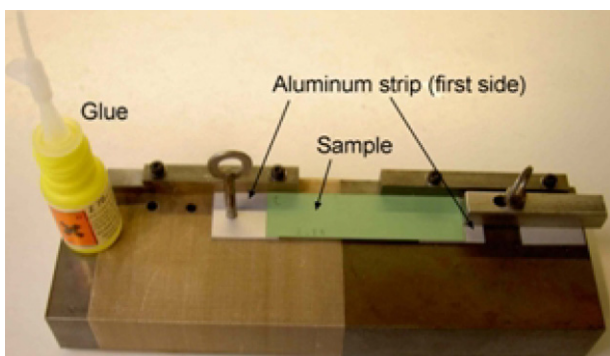

Fig. 3. Preparation of uniaxial tensile test specimens (6).

specimens were laser cut and polished to finish of 8.4 μm (using SiC paper 500, 1000 and 2400). Fig. 3 shows a setup of the sample mounting. The straps were made from two sandblasted aluminium strips of 25 mm × 20 mm × 1 mm with a 4 mm hole. These were glued on both sides of the specimen with contact glue (see Fig. 3). In the mounting of the samples the Instron machine pins are inserted through the 4 mm holes to insure no transfer of bending moment.

In order to minimize the stress concentrations at the straps, epoxy was filled into the corners. This was done to minimize stress concentrations, as the epoxy fillings provided a smooth transition from the cross section of the tested part of the specimen to the cross section of the specimen with straps.

The specimens were tested on an Instron machine with a 5 kN load cell, and the loading speed was 0.25 mm/min.

The Young's moduli of the uniaxial tension specimens were measured by the impulse excitation technique. This involved the use of a resonant frequency and a damping analyser (RFDA System 23 from IMCE NV, Genk, Belgium).[7] Impulse excitation offers fast and repeatable measurements of thin plates with a well defined geometry. The method is based on detecting characteristic vibration frequencies of simply supported specimens. The resonant frequencies of vibration are deduced from the digital signal by Fast Fourier Transform.

The Young's moduli of the laser cut uniaxial tensile test specimens with polished edges were determined by the impulse excitation technique prior to the strength testing by uniaxial tension. The dimensions (thickness, length and width) were measured by a digital vernier caliper and the weight of the specimens was measured by a Mettler Toledo digital gauge.

3. Mechanical analysis

3.1. Evaluation of stress

Evaluation of stress in the uniaxial tension experiments was done by dividing the force by the cross sectional area as the specimens only consist of one layer, i.e. the anode support.

For the ball-on-ring experiment the stresses were evaluated by using an analytical solution, which is based on classical laminate theory (see e.g. Ref. 8), and a solution to the elastic problem of a concentric loading ball and supporting ring.[9] The solution assumes small displacements, as well as linear elastic behavior for the material. This model can be found in Appendix A.

The disc shaped specimens were relatively thin compared to the support span and thus relatively flexible, that is why the deformations at failure were relatively large. This introduces redistribution of stresses, which cannot be described by the models relying on the assumption of small displacements. Therefore, the stresses were also evaluated by a large displacement finite element model (FEM) using the commercial code Comsol Multiphysics® 4.2 combined with Matlab® 6.5 for batch analysis.

In addition to the stresses that occur due to the transfer of external force through the specimen, the thermal expansions yield thermal stresses. These were also included in the calculations using a reference temperature of 1140 °C, which was
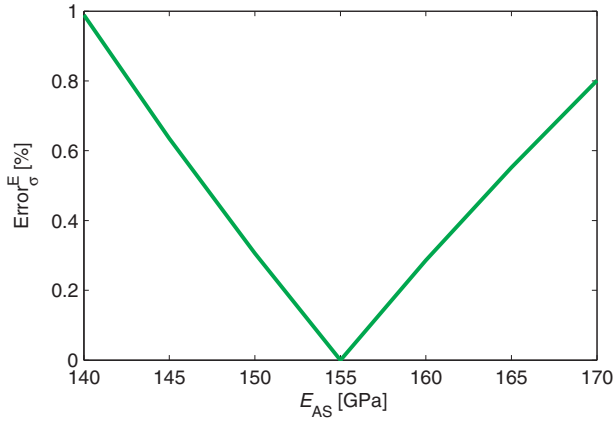
Fig. 4. An example of error on maximum stress in the sample under assumption of incorrect anode support stiffness (with 155 GPa as reference anode support stiffness). The thickness of the anode support and anode were set to 320 μm, and the electrolyte set to 10 μm, and the diameters of the ball, ring and disc were 2.78 mm, 16 mm, and 20 mm in the example, respectively.

obtained from the initial curvature of the cells (see Appendix A for further details).

3.2. Elastic parameters

The elastic material parameters are needed for the ball-on-ring stress evaluation (see Appendix A). For the ball-on-ring experiments the maximum stress at a given load level is relatively insensitive to the material parameters, even to the Young's modulus of the anode support.

To illustrate this, the error on the maximum stress given changes in elastic modulus from an assumed 'true' elastic modulus of 155 GPa is plotted in Fig. 4

$$\text{Error}_\sigma^E = \text{abs}\left(\frac{\sigma_{\max}(E) - \sigma_{\max}(155\,\text{GPa})}{\sigma_{\max}(155\,\text{GPa})}\right) \quad (1)$$

As seen in Fig. 4 modifying the elastic modulus up to 15% provides an error on the determined maximum stress to be less than 1.5%. Therefore, the elastic modulus was not measured for each sample, and the elastic material parameters were estimated from the porosity of the layers using the composite sphere model[5]

$$E = E_0 \frac{(1-p)^2}{1 + (2 - 3\nu_0)p} \quad (2)$$

$$\nu = \frac{1}{4} \frac{4\nu_0 + 3p - 7\nu_0 p}{1 + 2p - 3\nu_0 p} \quad (3)$$

where p is the porosity, E_0 and ν_0 are the elastic modulus and Poisson ratio at zero porosity. The two latter constants are provided in Table 2 for the main layers.

The Young's moduli of the specimens for the uniaxial test were calculated from the impulse excitation measurements. The method is described in ASTM E 1876-99 and ASTM C 1259 standards. When the fundamental resonance frequency, f_f, as

well as the mass, M, and the dimensions of the specimen are accurately known, the Young's modulus is calculated as

$$E = 0.9465 \cdot \frac{M f_f^2}{w} \frac{l^3}{t^3} T_1 \quad (4)$$

where w, l and t are the width, length and thickness of the beam, respectively, and T_1 a correction factor depending on the thickness-to-length ratio and Poisson ratio of the material. For the specimens here considered the thickness-to-length ratio is small (0.005–0.008) and the value of T_1 is very close to unity.

3.3. Statistical analysis

The failure in a ceramic component occurs due to a significant flaw at a high tensile stress, and consequently the distribution of flaws in the material results in a distribution of strength. In order to quantify this variation, a statistical analysis has been applied to represent the strength, and it is assumed that the strengths are Weibull distributed. The probability of failure P_f in the Weibull distribution at a given stress σ is calculated by

$$P_f = 1 - \exp\left(-\int_V \left(\frac{\sigma}{\sigma_0}\right)^m \frac{dV}{V_0}\right) \quad (5)$$

where m is the Weibull modulus and σ_0 is the Weibull strength in a reference volume V_0. Compressive stresses are not considered to contribute to the probability of failure, as the compressive strength is much higher than the tensile strength. Thus, we here define the strength as the largest occurring tensile stress, $\sigma_{\max}$, in a continuum sense. Eq. (5) is often re-written in terms of the strength in an efficient volume, V_{eff}, as follows

$$P_f = 1 - \exp\left(-\left(\frac{\sigma_{\max}}{\sigma_0}\right)^m\right) \quad (6)$$

where the efficient volume is equal to the reference volume, which then can be calculated from Eqs. (5) and (6) to

$$V_{\text{eff}} = V_0 \equiv \int_V \left(\frac{\sigma}{\sigma_{\max}}\right)^m dV \quad (7)$$

The efficient volume V_{eff} corresponds to the volume of a uniaxially tensed specimen with equal probability of failure as the ball-on-ring specimen.

The probability for larger flaws is higher in larger specimens, and thus the apparent strength is lower. Therefore, the strength must be related to the size of the specimen used for testing. This enables scaling up to the geometry and stress field of a real size cell. The scaling is based on the fact that the probability of failure for a given component is the same independent of which reference set of an efficient volume and Weibull strength is used. Thus, the probability of failure can be stated (in Eq. (5)) for two sets of efficient volume and Weibull strength to be equal

$$P_f = 1 - \exp\left(-\int_V \left(\frac{\sigma}{\sigma_0'}\right)^m \frac{dV}{V_{\text{eff}}'}\right)$$

$$= 1 - \exp\left(-\int_V \left(\frac{\sigma}{\sigma_0''}\right)^m \frac{dV}{V_{\text{eff}}''}\right) \quad (8)$$

Table 2
Elastic parameters and thermal expansion coefficient of the anode support and electrolyte layers.[10]

Layers	Material	E_0 [GPa]	ν_0	Porosity [%]	TEC [$\times 10^{-6}$ K^{-1}]
Electrolyte	TZ8Y	190	0.308	~0	10.8
Anode support	NiO–TZ3Y	217	0.333	Varies	13.1

from which the scaling rule for the Weibull strengths and efficient volumes can be derived as

$$\left(\frac{\sigma'_0}{\sigma''_0}\right)^m = \frac{V''_{\text{eff}}}{V'_{\text{eff}}} \tag{9}$$

The two Weibull parameters (σ_0 and m) were obtained by linearizing Eq. (6), subsequently fitting this to the set of measured strengths, $\sigma_{\text{max},i}$, and corresponding assigned probabilities of failure, $P_{f,i}$. The probability of failure for a set of measured strengths can be obtained by assigning the strength of each specimen to equal probability of occurrence. Thus, ordering the strength in ascending order $\sigma_{\text{max},1}, \sigma_{\text{max},2}, \ldots, \sigma_{\text{max},N}$ each strength is assigned a probability of failure

$$P_{f,i} = \frac{i - 0.5}{N} \quad i = 1, 2, \ldots, N \tag{10}$$

where N is the number of specimens. To achieve a low uncertainty, more than 30 specimens have been used for each tested series.[11]

The stress field in the ball-on-ring specimen is multi-axial, which is not necessarily the case for the stress field for the cells in operation. Thus, some generalization of the failure criteria is needed. Research on multi-axial failure criteria has been carried out by several authors, see e.g. Refs. 12–14. The failure criteria can be more or less sensitive to shear stresses, and this dependency has not yet been investigated for SOFC materials. Thus, the first principal stress, i.e. the largest tensile stress, is used in this work for the statistical analysis.

4. Results and discussion

4.1. Investigation of ball-on-ring stress evaluation method

In this section the accuracy of the different stress analysis methods used for the ball-on-ring experiment is investigated.

To compare the different solutions, the error of the maximum stress and the error on the maximum displacement in the analytical solution and the small displacement FEM solution are compared to the maximum stress in the more accurate large displacement solution for different load levels. The errors are thus defined as

$$\left. \begin{array}{l} \text{Error}_\sigma^\alpha = \text{abs}\left(\dfrac{\sigma_{\text{max}}^\alpha - \sigma_{\text{max}}^{\text{LD-FEM}}}{\sigma_{\text{max}}^{\text{LD-FEM}}}\right) \\\\ \text{Error}_w^\alpha = \text{abs}\left(\dfrac{w_{\text{max}}^\alpha - w_{\text{max}}^{\text{LD-FEM}}}{w_{\text{max}}^{\text{LD-FEM}}}\right) \end{array} \right\} \tag{11}$$

where LD-FEM is an abbreviation for large displacement FEM, and α denotes 'analytical solution' and 'small displacement FEM' the in turn.
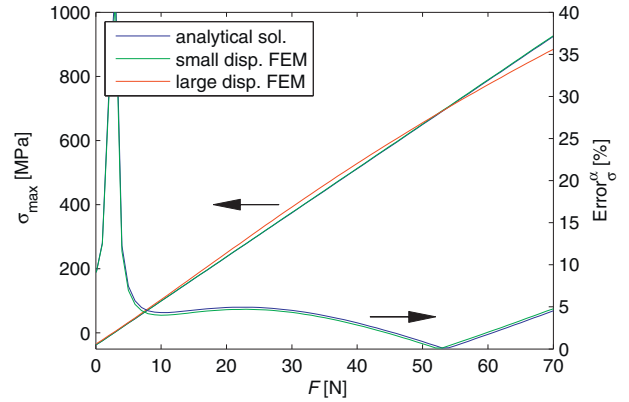

Fig. 5. Error (in %) on the maximum stress by using small displacement theories in relation to a large displacement FEM solution. The thickness of the anode support and anode were set to 320 μm, the electrolyte 10 μm, with ball, ring and disc diameters of 2.78 mm, 16 mm, and 20 mm, respectively.

The error on the maximum stress using an analytical solution and a small displacement FEM compared to a large displacement FEM can be seen in Fig. 5. As seen, the error is significant at small stresses, where the reference stress ($\sigma_{\text{max}}^{\text{LD-FEM}}$) is small, and the division of a number close to zero provides a large number for the error. The error is again higher at relevant larger load levels, with larger displacements. At the load level of approximately 2 N the maximum stress goes from negative to positive as the residual stress is exceeded by the stress from external loads. At this point Error$_\sigma^\alpha$ goes to infinity as the enumerator goes to zero. At 43 N the stresses in the large displacement FEM goes from being larger than those of the two others to smaller, and the error is consequently zero here. The reason for this is that stress field is changing shape. The stresses are changing from being bending (zero stress in the center) to be more equally distributed over the
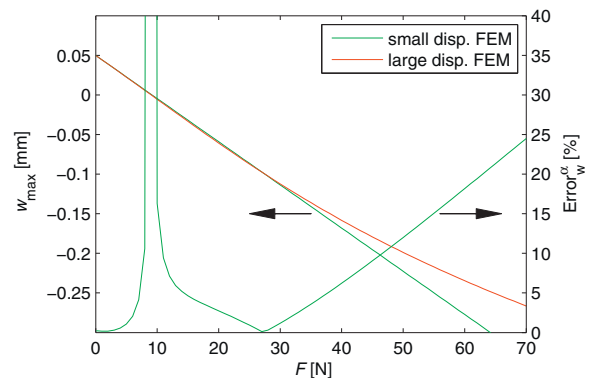

Fig. 6. Error on the maximum displacement by using small displacement theories in relation to a large displacement FEM solution. The thickness of the anode support and anode have been set to 320 μm, and the electrolyte 10 μm, and the dimensions of the ball, ring and disc 2.78 mm, 16 mm, and 20 mm, respectively.
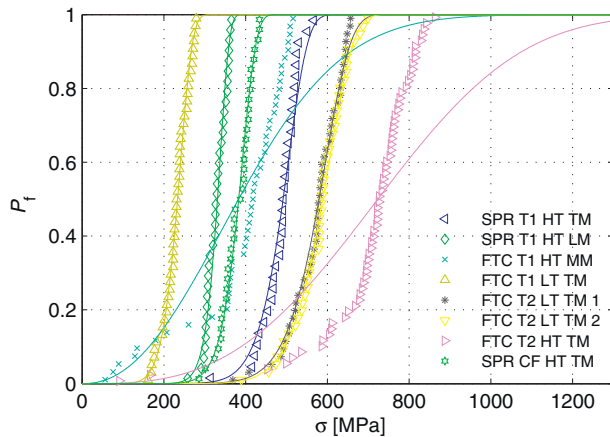
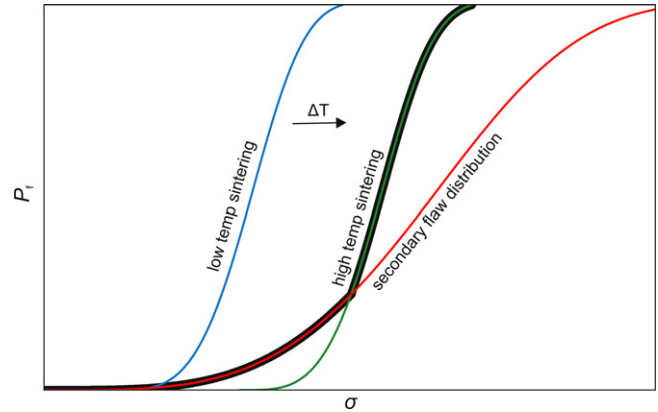Fig. 7. Probability of failure for the different test series.

Fig. 8. Overlapping failure distributions occurring at shifted strength distribution for increase sintering temperature. The particular overlap has only been observed with fully tape cast cells.

cross section due to the curvature (think of is as a balloon or a turned over dome).

The error on displacement in the small displacement FEM solution compared to the large displacement is shown in Fig. 6. To our best knowledge no analytical expression for the displacement exists, so only the small displacement solution has been compared to the large displacement solution. Again the displacement goes from an initial positive value due to residual stresses and becomes negative as the external load increases. And also here the large displacement FEM is initially larger in magnitude than that of the small displacement FEM, and a shift occurs at approximately 28 N. The error on the small displacement FEM displacements is much larger than that of the stresses as seen in Fig. 6. In the present investigation this does not influence the results, but greater care should be taken when choosing method for determining displacements.

In Table 3 the Weibull parameters of the strength distribution obtained by the three types of analysis are shown. These three types of analysis are with increasing accuracy; the analytical model in Appendix A, a small displacement FEM and large displacement FEM. There is a clear deviation of the solutions based on small displacement theory to the large displacement FEM solution. Thus, with the stress analysis in current setup should be analyzed with the large displacement FEM.

From this point onwards, only results obtained using large displacement FEM are shown.

The variation of the efficient volume in Table 3 can be ascribed to the variation in the Weibull modulus, which is used in the calculation of the efficient volume, according to Eq. (7).

4.2. Influence of half-cell assembly method

In addition to the Weibull parameters shown in Table 3, the entire data sets are plotted in Fig. 7 together with the fitted Weibull probability density functions. The fit of the two high temperature sintered fully tape casted half-cells measurements ("FTC T1 HT MM", "FTC T2 HT TM") was poor. The reason for this is illustrated in Fig. 8, where two overlapping failure distributions (the green and red lines) result in an efficient error distribution (black thick line). The secondary failure distribution

coincides with the full tape casting shaping technique and high temperature sintering, but were not identified. We speculate that this secondary flaw distribution is related to the edge defects and the residual stresses at the edge although we do not know for sure.

Removing the data points from the weaker specimens, which are believed to have failed because of an unidentified set of secondary flaws results in better fits of the Weibull distributions (see Fig. 9) together with higher Weibull moduli and similar Weibull strengths (see the ** marked results in Table 3).

4.3. Influence of porosity

Figs. 10 and 11 show two micrographs of the two test series "SPR T1 HT TM" and "SPR T1 HT LM", respectively. In Fig. 11 considerably larger grains can be seen in the anode support layer, and as seen in Table 1 the as-sintered porosity is also considerably higher (13.7% compared to 6.8%). The only difference between the two cells is the milling of the starting powders. In the former a larger amount of slurry has been milled for a shorter period. This has resulted in smaller grain sizes. The result of
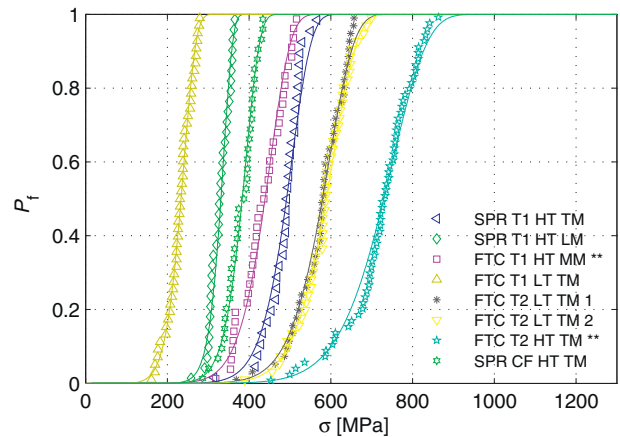

Fig. 9. Probability of failure for the different test series. The ** markers indicate that some of the weaker specimens have been removed from the test series (as discussed in the text).

Table 3
Calculation of Weibull parameters by three different methods with ascending order of accuracy.

Test code	Analytical solution		Small disp. FEM		Large disp. FEM			Numb of spec., N
	σ_0 [MPa]	m	σ_0 [MPa]	m	σ_0 [MPa]	m	V_{eff} [mm³]	
SPR T1 HT TM	490	10.9	491	10.9	508	11.3	0.041	33
SPR T1 HT LM	322	15.6	323	15.6	339	15.7	0.024	36
FTC T1 HT MM	433	2.2	434	2.2	452	2.2	1.517	47
FTC T1 HT MM[b]	438	9.4	439	9.4	456	9.8	0.051	39
FTC T1 LT MM	231	9.0	232	9.0	243	8.9	0.006	49
FTC T2 LT TM 1	587	9.7	588	9.7	600	10.4	0.045	48
FTC T2 LT TM 2	591	10.3	592	10.3	609	10.9	0.043	48
FTC T2 HT TM[a]	803	3.0	805	3.0	817	3.0	0.611	64
FTC T2 HT TM[b]	748	8.9	751	8.9	758	9.6	0.054	62
SPR CF HT TM	380	11.7	381	11.7	395	12.4	0.024	37

[a] ~7 specimens broke before being tested (not included in statistics).
[b] Weakest specimens neglected (discussed below). Marked with ** in the figures.
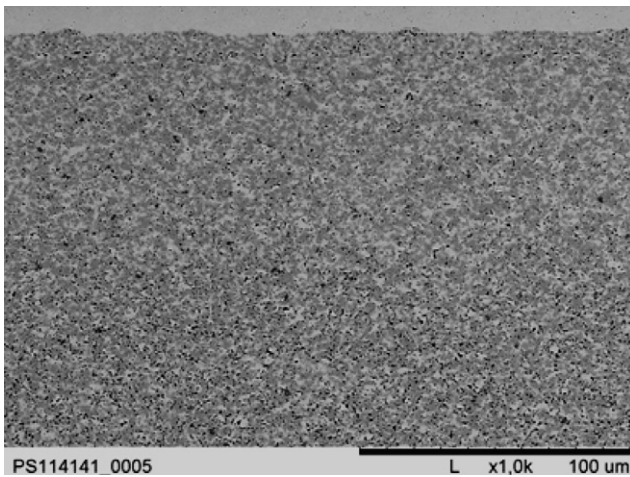

Fig. 10. SEM micrograph of a cell cross-section showing electrolyte and anode support of standard sprayed half-cell from the "SPR T1 HT TM" test series.

the "light" milling is however clear, i.e. a drop of the Weibull strength of 34% from 517 MPa to 339 MPa.

The influence of the powder milling should always be considered in connection with the sintering conditions. The weakest measured cells were manufactured using reasonable milled powders, which usually results in intermediate porosity. However
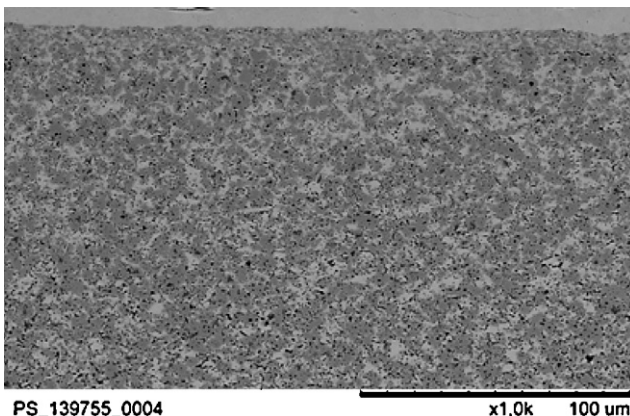

Fig. 11. Micrograph of electrolyte and anode support of standard sprayed half-cell from the "SPR T1 HT LM" test series.

they were sintered at a relatively low temperature for the specific material system (T1), resulting in very high porosity (17.4%).

That porosity can influence Weibull strength of a material is expected, as less material is available to transfer external forces resulting in higher local stresses. The cells in this work were, as previously described, manufactured with variation in processing parameters such as milling times, sintering temperatures, shaping technique and material systems, with consequent different distributions and spatial distribution of pores in the anode supports (see Figs. 10 and 11). However, in spite of all these different variations, which all have a potential impact on strength, a very strong dependency of Weibull strength on total as-sintered porosity was found as illustrated in Fig. 12.

Furthermore, the Weibull strength decreases relatively fast with increasing porosity. Within the interval of commonly used porosities, i.e. 10–15%, the Weibull strength varies from approximately 500 MPa to 300 MPa. This is a rather large variation of strength to account for in the design of a stable and durable system.

Typically, the dependency of the strength on porosity is fitted with the following two parameter exponential expression,[15] which leads to the curve shown in Fig. 12

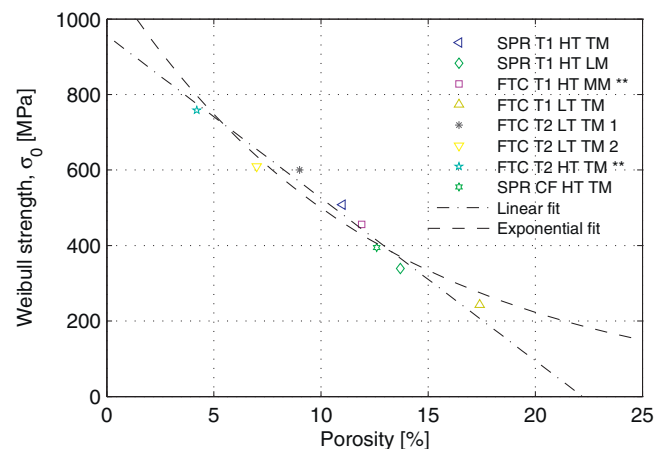$$\sigma = \tilde{\sigma} \exp(-bp) \tag{12}$$

Fig. 12. Measured Weibull strength as a function of the porosity in the ball-on-ring experiments.
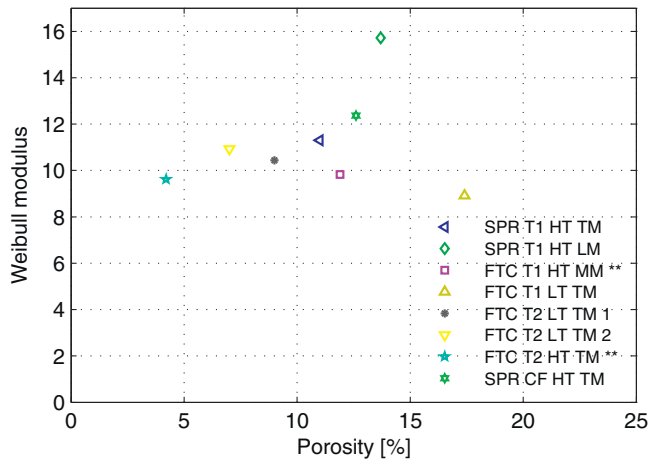
Fig. 13. Porosity and Weibull modulus for the cells in the ball-on-ring experiments.

Fig. 14. Variation of Young's modulus (○) and strength (×) with porosity in the uniaxial tension experiments.

where $\tilde{\sigma}$ is the strength at zero porosity, which have been fitted to 1118 MPa. The parameter b indicates the dependency on porosity; and the larger the b, the stronger the dependency. For the current experiments b was determined to be 8.0.

The consequence of this high dependency is that the probability of failure of a stack is very sensitive to the porosity. Thus, it is a parameter that needs to be controlled accurately for minimization of the cost of the technology (discussed further below). The consequence of not doing so is the need for conservative design and operation of SOFC stacks. This again entails smaller thermal loads and restrictions on the flow configurations and fuel utilizations. For optimization of SOFC stack designs towards durability, minimization of strength variations, and consequently porosity variations should be in focus. The strength should be tested continuously in the production, or alternatively monitored via the porosity as these results here suggest.

As seen in Fig. 13 there is a tendency for Weibull modulus to increase slightly with increasing porosity, but the tendency is much less clear than that found for Weibull strength. Further investigations must be carried out to verify this. If this is the case it means that the critical flaws are more uniformly distributed at higher porosities.

4.4. Comparison with uniaxial tension and IET

The results above showing the high dependency of Weibull strength on porosity ($b = 8.0$) are unusual and an extra independent set of experiments has been conducted to verify this. The strength was measured by uniaxial tension and the result is shown in Fig. 14. Here there is also a tendency of the strength to vary with porosity. However each point is represented by only one sample compared to the previously used Weibull strength of more than 30 specimens. Therefore a far greater scatter is seen. Fitting the exponential expression in Eq. (12) yields $b = 7.6$, which is in good agreement with previously obtained $b = 8.0$ for the ball-on-ring experiment.

The strength obtained in these experiments can be compared to the Weibull strength in the ball-on-ring experiment using
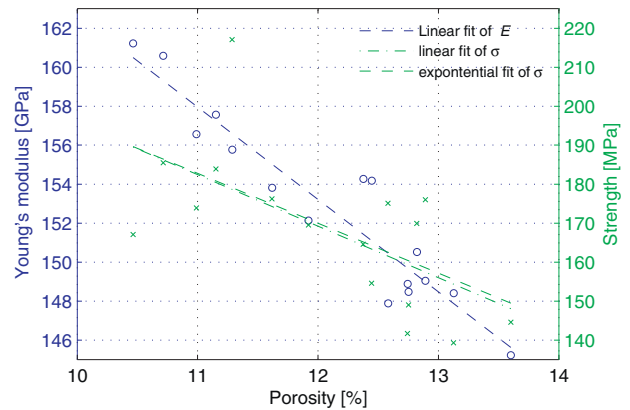
Eq. (9). This is done in the following to investigate the validity of Weibull strength scaling with efficient volume.

Here we choose the strength at 11% porosity for comparison. The Weibull strength at 11% porosity in the ball-on-ring experiment can be calculated to 461 MPa from the exponential fit. In the scaling an efficient volume of 0.041 mm^3 is chosen for the ball-on-ring. The efficient volume of the uniaxial tension experiment is 390 mm^3, when the volume of the area with straps ($2 \text{ mm} \times 5 \text{ mm}$) is subtracted (($70–10$) mm $\times$ 20 mm $\times$ 0.325 mm). The Weibull strength at 390 mm^3 can then be calculated to

$$\sigma_0' = 461 \text{ MPa} \left(\frac{0.041 \text{ mm}^3}{390 \text{ mm}^3} \right)^{1/11} = 200 \text{ MPa} \qquad (13)$$

The linear regression performed in Fig. 14 provides the mean values, so for a comparison the Weibull strength of 200 MPa should be converted to the mean strength. Calculating the mean strength, σ_{50}, from the Weibull strength can be done by setting the probability of failure equal to 50% and solving for the stress in Eq. (6)

$$\sigma_{50} = 200 \text{ MPa} \left(-\ln(0.5) \right)^{1/11} = 193 \text{ MPa} \qquad (14)$$

Comparing the 193 MPa to the 158 MPa shows a deviation of about 23%, which is a significant deviation. Thus, it can be concluded that these simple models cannot account for all the complexities in the multi-axial stress field, the volume scaling of several magnitudes or another unknown phenomena. It should be noted that this does not disprove the Weibull efficient volume scaling methodology, as it actually captures the tendency of more than doubling the strength by going from the larger to the much smaller efficient volume.

The samples for uniaxial tension were also suitable for measuring the Young's moduli by IET. The Young's modulus is an integrated continuum descriptor (average) of the sample as the porosity in opposition to the strength, which is dependent on local flaws. Therefore a better correlation is found between the porosity and the Young's modulus as seen in Fig. 14. This finding is very interesting as it opens to the opportunity for non-destructive testing and quality control in the production of the cells by IET.
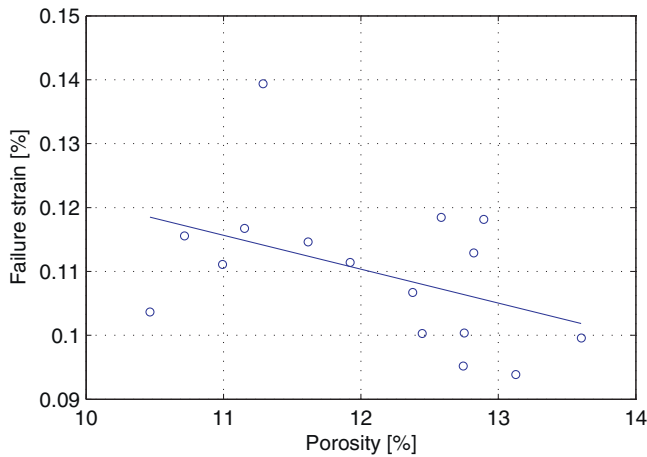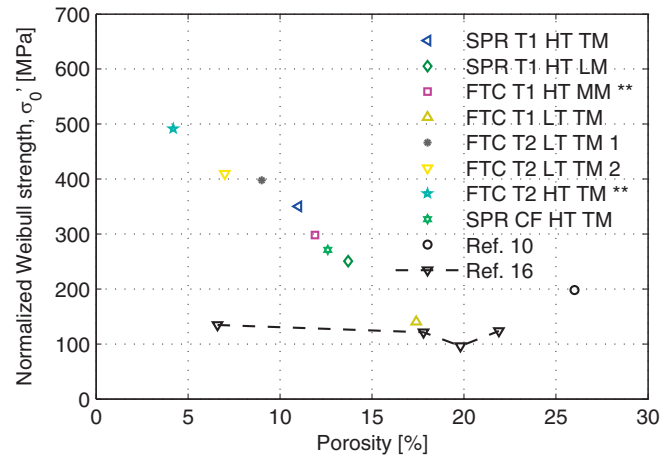
Fig. 15. Variation of failure strain with porosity.

Fig. 16. Weibull strengths at different porosities in present work and Refs. 10 and 16 scaled to an efficient volume of 1 mm^3 by Eq. (9).

Finally the connected strength and stiffness measurements allow for the investigation on the failure strain ($\varepsilon_u = \sigma_u/E$). As seen in Fig. 15 the variation of strength introduces a scatter on the result, but the failure strains are about 0.11% and have a tendency to decrease for increasing porosities.

4.5. Comparison with other measurement

Table 4 shows the results obtained by Atkinson and Selcuk[10] and Radovic and Lara-Curzio.[16] The Weibull strengths of these measurements are scaled to an efficient volume of 1 mm^3 by Eq. (9) to be able to compare the measurements, and this Weibull strength is here denoted σ_0^I.

Fig. 16 shows the Weibull strengths obtained in the present work (see Table 3), scaled to an efficient volume of 1 mm^3, as well as those reported in the literature and shown in Table 4. The specimens in the present work can be seen to be significantly stronger than those reported in the literature. This is most likely due to the type of YSZ as NiO–8YSZ was used in Refs. 10 and 16, and transformation NiO–3YSZ[17] was used for the cells in the present study.

Furthermore, notice that the decrease of Weibull strength with porosity in 16 is much smaller ($b = 2.6$). In general the decrease of strength with porosity observed for the anode supports of this work is quite high in comparison to other porous ceramics, where b typically varies between 3 and 6 with the exception of $b = 7$ for β-Al$_2$O$_3$.[15]

The fact that the decrease of the Weibull strength is higher for NiO–3YSZ could be a side effect of the transformation toughening of the 3YSZ backbone. The toughening mechanism stems from a volume expansion and the consequent compressive stress build up at the crack tip from displacement restrictions by ambient material. If some of the ambient material is removed and replaced by porosity the toughening mechanism would decrease. Thus, NiO–3YSZ anode support with increasing porosity may suffer from both introduction of larger flaws and a gradual loss of the toughening mechanism. This could be investigated by micro-structural fracture mechanical model.

4.6. Optimization of porosity

To optimize the strength the porosity should be minimized. However the anode supports are not only required to be strong but also be able transport the fuel gasses to the active sites in the anode. For this purpose the porosity should be maximized. Hence, an optimal porosity must exist, and could be obtained by weighing the strength against performance and durability. The challenge here is to determine the weight factors for each contributing parameter. Here the mathematical frame for such an optimization of the porosity in a SOFC system is presented. The purpose is not to provide an optimal porosity, as this will depend on the specific system design.

Table 4
Weibull strength, Weibull modulus, efficient volume and porosity from other measurements on NiO–YSZ in the literature. σ'_0 denotes the Weibull strength scaled to an efficient volume of 1 mm^3 and N the number of specimens.

Ref.	Material	σ_0 [MPa]	m	V_{eff} [mm^3]	p [%]	σ'_0 [MPa]	N
10	NiO–8YSZ	187	11.8	1.95[b]	26[a]	198	10
16	NiO–8YSZ	135	8.6	0.99[b]	6.6	135	15
		98	4.3	2.54[b]	17.8	121	15
		92	6.8	1.35[b]	19.8	96	15
		95	4.0	2.80[b]	21.9	123	15

[a] Private communication.
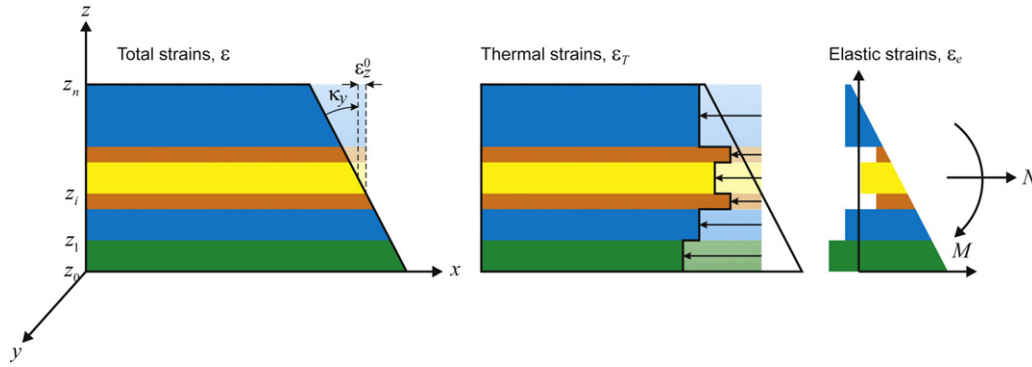[b] Estimated from the approximate dimensions found in the references.

Fig. 17. Cross section of a deformed multi-layer structure. The total strain is divided into thermal strains and elastic strains. The pale colored parts indicate the original shape.

This object can be approached by expressing the total earnings, Earn, as the earning by production of electricity subtracted the initial cost, $Cost_{ini}$, and the cost of replacing the failing systems, $Cost_{ini} \cdot P_f$

$$\text{Earn} = \int_0^{t_{life}} (\text{Price}_{el} - \text{Price}_{fuel}) \cdot \text{Efficiency} \cdot dt$$
$$- \text{Cost}_{ini} - \text{Cost}_{ini} \cdot P_f \qquad (15)$$

where probability of failure, P_f, and efficiency depends on porosity. The probability of failure depends on the porosity via the Weibull strength (Eq. (5)), and the efficiency depends on the porosity and the degradation rate, which may also depend on porosity

$$\text{Efficiency} = \text{Efficiency}_{ini} \, (1 - \text{Degradation}) \qquad (16)$$

The optimization for the porosity can then be stated as the minimum of Eq. (15)

$$\frac{\partial \text{Earn}}{\partial p} = \frac{\partial \int_0^{t_{life}} (\text{Price}_{el} - \text{Price}_{fuel}) \cdot \text{Efficiency} \cdot dt}{\partial p}$$
$$- \text{Cost}_{ini} \cdot \frac{\partial P_f}{\partial p} = 0 \qquad (17)$$

Other factors such as redox stability[18,19] and degradation in the form of, e.g. Nickel coarsening[20] or impurity segregation[21,22] also change with porosity and influence the 'Efficiency'. These effects can also be included in the framework.

5. Conclusions

In this work the strength of solid oxide half-cells, or individual anode support layers, was studied upon changes to various processing parameters; i.e. material system, milling, assembly method, and sintering temperature. The strength of the anode supports was measured by the ball-on-ring method. The stresses in the ball-on-ring method were analyzed by three methods with increasing accuracy: an analytical expression, small displacement finite element analysis and large displacement finite element analysis. The variation of strengths was described by

Weibull theory, and the Weibull parameters were obtained by linear regression. Following findings were made:

- With the applied dimensions of the test setup (diameter of ring = 16 mm, and thickness of specimens $\approx 325 \, \mu$m) and load level (≈ 40 N), an error of approximately 5% is committed by application of small displacement theories. It is therefore recommended that large displacement finite element analysis is applied for higher accuracy.
- For the test series made with higher sintering temperatures and full tape-casting a secondary flaw distribution was believed to appear. This was seen as a few much weaker samples in the lower tale of the strength distribution. Hence, the strength distribution could not be fitted with a single Weibull expression. Removing those few very weak samples provided good Weibull fits. The secondary flaw distribution was not discovered.
- A high correlation between Weibull strength and porosity was obtained. Thus, the variation of the Weibull strengths can, to a significant extent, be represented by the resulting porosity independent of the processing parameter varied.
- The Weibull modulus was also found to correlate with the porosity. The higher the porosity the higher the modulus.
- The dependency of Weibull strength on the total porosity was found to be relatively strong. For instance, a variation of porosity from 10% to 15% lowered the strength by approximately 40%. This decrease in strength with porosity was found to be higher than that observed for other ceramic materials. The effect was speculated to be due to a weakening of the effect of the phase transformation of the partially stabilized tetragonal Zirconia.

To verify this unusually strong dependency of the strength on porosity another set of experiments were carried out where the strength, porosity and stiffness were measured on each sample by uniaxial tension and the impulse excitation technique. The following was found:

- The same high decrease of strength with porosity as in the ball-on-ring measurements.

- The scaling of Weibull strength from low to high efficient volume provided an error of approximately 20%. It is a high deviation, which is speculated to be due to the different stress fields in the two test methods and the uncertainty of edge effects in the uniaxial tension case.
- That the porosity correlates very well to the stiffness, which can be measured by the non-destructive impulse excitation technique. This opens for the opportunity of non-destructive quality testing in the production.

Finally, it is suggested how this finding of a decrease in strength with porosity can be taken into consideration in the design of a SOFC system, by applying classical optimization methods.

Acknowledgements

$$N = \int_{z_0}^{z_1} \sigma dz + \ldots + \int_{z_{i-1}}^{z_i} \sigma dz + \ldots + \int_{z_{n-1}}^{z_n} \sigma dz = \sum_{i=1}^{n} \int_{z_{i-1}}^{z_i} \sigma dz$$
$$M = \int_{z_0}^{z_1} \sigma z dz + \ldots + \int_{z_{i-1}}^{z_i} \sigma z dz + \ldots + \int_{z_{n-1}}^{z_n} \sigma z dz = \sum_{i=1}^{n} \int_{z_{i-1}}^{z_i} \sigma z dz \quad \left.\right\} \quad (25)$$

Appendix A.

The strain ε is divided into to two contributions, i.e., elastic strain ε_e and thermal strain ε_T

$$\varepsilon = \varepsilon_e + \varepsilon_T \quad (18)$$

whereby creep strain, strains due to reactions etc. are neglected.

The thermal strain in the ith layer can be calculated by

$$\varepsilon_{T,i} = -\int_{T_{\text{ref}}}^{T} \alpha_i(T) dT \quad (19)$$

where $\alpha_i(T)$ is the thermal expansion coefficient of the ith layer. T_{ref} is the so-called reference temperature or zero stress temperature. This is the fictive temperature from which thermal stresses are building up. In reality such a temperature does not exist, since a temperature regime, where both thermal stresses are build up and creep occur, exists. For a pure elastic calculation of stress at room temperature no errors are committed by this approach.

Assuming a constant or an average thermal expansion coefficient through the considered temperature interval simplifies (19) to

$$\varepsilon_{T,i} = \alpha_i(T - T_{\text{ref}}) \quad (20)$$

For long and slender structures as the cells considered in this work, the Bernoulli assumption, i.e. plane cross-sections remain plane, provides good results, and the strain field can be described by a linear expression

$$\varepsilon = \varepsilon^0 + \kappa z \quad (21)$$

where ε^0 is the average expansion, κ is the curvature, and z is the coordinate orthogonal to the plane of the layers (Fig. 17).

The normal force N is obtained as the integral of the normal stresses in a cross section through the layers

$$N = \int_{z_0}^{z_n} \sigma dz \quad (22)$$

and the bending moment M as the first moment of the normal stresses

$$M = \int_{z_0}^{z_n} \sigma z dz \quad (23)$$

For the ith layer in a multi-layered structure the elastic constitutive law can be written as

$$\sigma = \frac{E_i}{1 - \nu_i} \varepsilon_e \quad (24)$$

Integration of the stresses of the layers is provided by (22) and (23) provides the normal force and the bending moment

which simplifies to

$$N = \sum_{i=1}^{n} \int_{z_{i-1}}^{z_i} \frac{E_i}{1 - \nu_i} (\varepsilon^0 + \kappa z - \varepsilon_{T,i}) dz$$
$$M = \sum_{i=1}^{n_p} \int_{z_{i-1}}^{z_i} \frac{E_i}{1 - \nu_i} (\varepsilon^0 + \kappa z - \varepsilon_{T,i}) z dz \quad \left.\right\} \quad (26)$$

Assuming constant temperature throughout the layers and thus equal thermal strain in each layer ($\varepsilon_{T,i}$) allows for further simplification of (26) to

$$N = A\varepsilon^0 + B\kappa - N_T$$
$$M = B\varepsilon^0 + D\kappa - M_T \quad \left.\right\} \quad (27)$$

where

$$A = \sum_{i=1}^{n} \frac{E_i}{1 - \nu_i} (z_{i-1} - z_i)$$
$$B = \sum_{i=1}^{n} \frac{E_i}{1 - \nu_i} \frac{z_{i-1}^2 - z_i^2}{2}$$
$$D = \sum_{i=1}^{n} \frac{E_i}{1 - \nu_i} \frac{z_{i-1}^3 - z_i^3}{3} \quad \left.\right\} \quad (28)$$

$$N_T = \sum_{i=1}^{n} \int_{z_{i-1}}^{z_i} \frac{E_i}{1-v_i} \varepsilon_{T,i} dz$$
$$M_T = \sum_{i=1}^{n} \int_{z_{i-1}}^{z_i} \frac{E_i}{1-v_i} \varepsilon_{T,i} z dz \quad\quad (29)$$

The distribution of the bending moment in the ball-on-ring setup is

$$M = \frac{F(1+v)}{8\pi} \times Q(r) \quad\quad (30)$$

where $Q(r)$ is a geometry dependent function of the radial coordinate, r, which for the disc loaded in the ball on ring setup, is

$$Q(r) = \begin{cases} 1 + 2\ln\left(\dfrac{a}{b}\right) + \dfrac{1-v}{1+v}\left(1 - \dfrac{b^2}{2a^2}\right)\dfrac{a^2}{R^2} & \text{for} \quad 0 \le r < b \\ 2\ln\left(\dfrac{a}{r}\right) + \dfrac{1-v}{1+v}\left(\dfrac{1}{2} - \dfrac{b^2}{2a^2}\right)\dfrac{a^2 b^2}{r^2 R^2} & \text{for} \quad b \le r \le a \end{cases} \quad (31)$$

where a, b and R are the radiuses of the ring, ball and disc, respectively.[9]

The normal force N in the ball-on-ring setup equals 0. The average expansion and the curvature are obtained from (27) to

$$\varepsilon^0 = \frac{DN_T - B(M_T + M)}{AD - B^2}$$
$$\kappa = \frac{-BN_T + A(M_T + M)}{AD - B^2} \quad\quad (32)$$

From this the strain can be calculated by (21), and then the elastic strain by (18) and finally the stress by (24).

The zero stress temperature T_{ref} can be obtained from the initial curvature before loading and solving Eq. (32) for it. T_{ref} enters Eq. (32) through N_T and M_T.

References

1. Yokokawa H, Tu H, Iwanschitz B, Mai A. Fundamental mechanisms limiting solid oxide fuel cell durability. *J Power Sources* 2008;**182**:400–12.
2. Hagen A, Liu YL, Barfod R, Hendriksen PV. Anode supported solid oxide fuel cells—deconvolution of degradation into cathode and anode contributions. *Solid Oxide Fuel Cells 10 (Sofc-X)* 2007;**7**(Pts 1 and 2):301–9.
3. Atkinson A, Selcuk A. Mechanical properties of ceramic materials for solid oxide fuel cells. In: *Proceedings of the fifth international symposium on solid oxide fuel cells (Sofc-V), vol. 97*. 1997. p. 671–80.
4. Malzbender J, Steinbrech RW. Fracture test of thin sheet electrolytes for solid oxide fuel cells. *J Eur Ceram Soc* 2007;**27**:2597–603.
5. Ramakrishnan N. Effective elastic moduli of porous solids. *J Mater Sci* 1990;**25**:3930–7.
6. Faes A, Frandsen HL, Kaiser A, Pihlatie M. Strength of anode-supported solid oxide fuel cells. *Fuel Cells* 2011.
7. Roebben G, Bollen B, Brebels A, Van Humbeeck J, Van der Biest O. Impulse excitation apparatus to measure resonant frequencies, elastic moduli, and internal friction at room and high temperature. *Rev Sci Instrum* 1997;**68**:4511–5.
8. Agarwal BD, Broutman LJ, Chandrashekhara K. *Analysis and performance of fiber composites*. Wiley-Interscience; 2006. p. 576.
9. Kirstein AF. Symmetrical bending of thin circular elastic plates on equally spaced point supports. *J Res Natl Bur Stand C Eng Instrum* 1967;**71C**:1–10.
10. Atkinson A, Selcuk A. Mechanical behaviour of ceramic oxygen ion-conducting membranes. *Solid State Ionics* 2000;**134**:59–66.
11. Khalili A, Kromp K. Statistical properties of Weibull estimators. *J Mater Sci* 1991;**26**:6741–52.
12. Andreasen JH. Statistics of brittle failure in multiaxial stress states. *J Am Ceram Soc* 1993;**76**:2933–5.
13. Batdorf SB, Heinisch HL. Weakest link theory reformulated for arbitrary fracture criterion. *J Am Ceram Soc* 1978;**61**:355–8.
14. Lamon J, Evans AG. Statistical-analysis of bending strengths for brittle solids—a multiaxial fracture problem. *J Am Ceram Soc* 1983;**66**:177–82.
15. Rice RW. *Porosity of ceramics*. New York: Marcel Dekker, Inc.; 1998.
16. Radovic M, Lara-Curzio E. Mechanical properties of tape cast nickel-based anode materials for solid oxide fuel cells before and after reduction in hydrogen. *Acta Mater* 2004;**52**:5747–56.
17. Hannink RHJ, Kelly PM, Muddle BC. Transformation toughening in zirconia-containing ceramics. *J Am Ceram Soc* 2000;**83**:461–87.
18. Pihlatie M, Ramos T, Kaiser A. Testing and improving the redox stability of Ni-based solid oxide fuel cells. *J Power Sources* 2009;**193**:322–30.
19. Faes A, Fuerbringer J, Mohamedi D, Hessler-Wyser A, Caboche G, Van Herle J. Design of experiment approach applied to reducing and oxidizing tolerance of anode supported solid oxide fuel cell. Part I: Microstructure optimization. *J Power Sources* 2011;**196**:7058–69.
20. Ramos T, Thydén K, Mogensen M. Electrochemical characterization of Ni/(Sc)YSZ electrodes. In: Mogensen M, Armstrong T, Gür T, Yokokawa H, editors. *ECS transactions*. 2010. p. 123–39.
21. Hauch A, Mogensen M. Ni/YSZ electrode degradation studied by impedance spectroscopy: effects of gas cleaning and current density. *Solid State Ionics* 2010;**181**:745–53.
22. Hansen KV, Norrman K, Mogensen M. H_2–H_2O–Ni–YSZ electrode performance—effect of segregation to the interface. *J Electrochem Soc* 2004;**151**:A1436–44.